Reprinted from Optical Mapping of Cardiac Excitation and Arrhythmias, D.S Rosenbaum and J. Jalife, Eds. 2001 with permission of the publisher, Futura Publishing Co., Inc., New York.

Chapter 19

New Perspectives in Electrophysiology from the Cardiac Bidomain

Shien-Fong Lin and John P. Wikswo, Jr.

Introduction

For many years, the uniform double layer model was widely accepted and used to describe the macroscopic electrical behavior of cardiac tissue. It predicted that outside a closed wave front, there should be no extracellular potential. In 1977, Corbin and Scher[1] measured the extracellular potential outside an expanding wave front and found a positive potential parallel to the fibers and a negative potential perpendicular to them. This observation was inconsistent with the uniform double layer model, and implied that a new and more general model was required to accurately relate the extracellular and transmembrane potentials. Corbin and Scher explained their results in terms of nonuniform dipole strength within the wave front, with the individual dipoles aligned with the fiber axis. Colli-Franzone and colleagues[2] developed an oblique dipole model to explain the experimental data.

An alternative model, with few ad-hoc assumptions, is the bidomain model, in which a 3-dimensional electrical cable represents the cardiac syncytium with distinct intracellular and extra cellular spaces separated by cell membrane.[3–11] The bidomain model treats the macroscopic heart as a continuous, nonlinear, 3-dimensional cable, with the effects of intercellular junctions incorporated into the anisotropic intracellular conductivities. As shown in Figure 1, this view is supported by the fact that the intracellular spaces of all cardiac cells are connected together sufficiently tightly through the gap junctions in the intercalated disks to form a 3-dimensional syncytium that can carry currents and support voltage gradients in all directions. Similarly, the cells share a common extracellular space that also forms a 3-dimensional conductor. Because of the tissue architecture, the electrical conductivities of the intracellular and extracellular spaces are directionally dependent, i.e., anisotropic, such that each domain in the model has its own anisotropic electrical resistivity. This also leads to the well-known anisotropic conduction velocity. At present,

From Rosenbaum DS, Jalife J (eds): *Optical Mapping of Cardiac Excitation and Arrhythmias.*

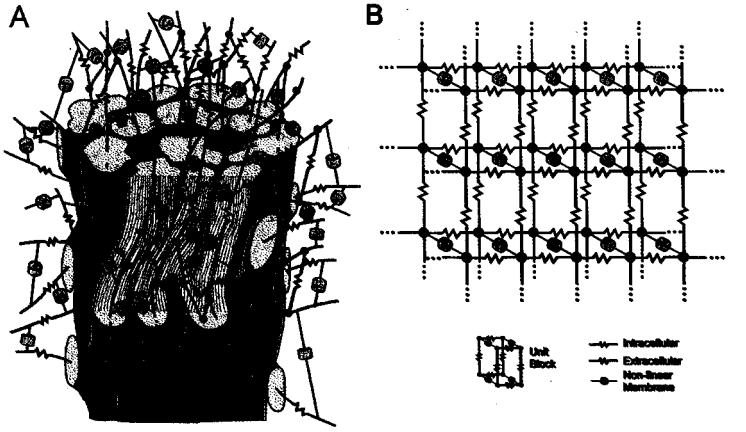

Figure 1. Schematic representation showing how the syncytial nature of cardiac tissue can be represented by a 3-dimensional coaxial cable. Intracellular (red) and extracellular spaces (blue) are represented by a pair of superimposed, 3-dimensional resistor arrays that are interconnected by the nonlinear membrane, represented by the yellow cylindrical elements. **A.** Irregular bidomain reflecting actual cardiac cellular structure. *Bottom:* Cardiac cells (red) are surrounded by the extracellular space (blue). *Middle:* Equivalent resistor network is superimposed on the cell structure, with the intracellular resistor network in red and the extracellular network in blue. The two are connected by the yellow nonlinear membrane elements. *Top third:* The resistor and membrane network is shown alone. Such cellular-scale bidomain models have yet to be implemented. **B.** A regular, 2-dimensional bidomain suitable for numerical calculations; the entire pattern can be translated out of the page to create a 3-dimensional bidomain. The choice of the resistors would define the fiber direction, in that the intracellular resistance would be 10 times greater across the fibers than along them for a 10:1 intracellular anisotropy ratio; the extracellular anisotropy would be 4:1. Typically, one element of a 3-dimensional bidomain mesh would be 100 μm to 1 mm on a side and, as such, would represent a large number of individual cardiac cells.

the complicated heterogeneous geometry in Figure 1A is homogenized to form the idealized, locally homogeneous, and highly regular bidomain seen in Figure 1B.

Mathematically, the bidomain model accounts fully for the syncytial nature of cardiac tissue, including the effects of tissue anisotropy, using a pair of coupled, partial differential equations governing the intracellular, V_i, and extracellular, V_e, potentials

$$\nabla \cdot \sigma_i \nabla V_i = \beta(C_m \partial V_m/\partial t + J_{ion}) - I_i$$

$$\nabla \cdot \sigma_e \nabla V_e = -\beta(C_m \partial V_m/\partial t + J_{ion}) - I_e$$

where σ_i and σ_e are the anisotropic electrical conductivity tensors of the two spaces (S/m), C_m is membrane capacitance per unit area (F/m^2), β is

the ratio of cell membrane area to tissue volume (m^{-1}), J_{ion} is the membrane ionic current per unit area (A/m^2), and I_i and I_e are the intracellularly and extracellularly applied external current sources per unit volume (A/m^3).

While these equations are easier to solve if the anisotropies of the intracellular and extracellular space are assumed to be the same, the physiologically realistic values for the tissue resistivities show the intracellular resistivity transverse to the fiber direction to be 10 times that of the resistivity along the fibers, for an intracellular anisotropy ratio of 10 to 1, while the ratio for the extracellular space is 4 to 1.[8,12,13] When the bidomain model has equal anisotropy ratios for the intracellular and extracellular spaces, it predicts zero extracellular potential outside a closed wave front, just as does the uniform double layer. However, if the two spaces are assigned the physiologically realistic, differing anisotropy ratios, the model predicts a variety of unexpected and interesting effects. In 1987, we showed that for a model with unequal anisotropy ratios, the extracellular potential is qualitatively similar to that observed by Corbin and Scher, with a region of positive extracellular potential leading the wave front in the direction along the fibers.[12]

Another implication of the bidomain model, first reported by Plonsey and Barr,[8] is that the intracellu lar and extracellular action currents associated with an expanding wave front are not equal and opposite. Rather, they form closed loops of net current with a fourfold (quatrefoil) symmetry. We realized that these current loops produce a magnetic field, whose quatrefoil pattern provides a unique signature of wave front propagation,[12] and that current injection produces a similar but quantitatively different pattern.[10] We have measured this magnetic field pattern using a high spatial resolution superconducting quantum interference device (SQUID) magnetometer scanned over a tissue slice from a dog heart.[14] Measurement of the magnetic field is a particu larly sensitive test of the bidomain model and unequal anisotropy ratios, because in the limit of equal anisotropy ratios, the magnetic field vanishes.

The doubly anisotropic bidomain model was rarely used to study electrical stimulation of cardiac tissue prior to 1989, when we calculated the transmembrane potential induced in a 2-dimensional bidomain stimulated with a unipolar electrode.[10] For strong stimuli, the boundary of the depolarized tissue under the cathode (the virtual cathode) has a complex, "dog-bone" shape that results in the wave front originating farther from the cathode in the direction perpendicular to the fibers than in the direction parallel to them. Concurrent with this theoretical study, we measured the virtual cathode size and shape in a dog by back-extrapolating the extracellular action potential wave front measurements to their site of origin.[15] We found a dog-bone-shaped virtual cathode that increased in size as the stimulus strength increased and was similar in shape to that predicted by the bidomain model.[16] The observed virtual cathode shape is sensitive to the tissue and membrane electrical properties and may provide a way to assess the effects of different drugs on cardiac tissue.[17] However, it was not until the widespread use of epifluorescence imaging of the transmembrane potential that the role of virtual cathodes and virtual anodes, and hence the importance of the complexity introduced by the unequal anisotropy ratios, became widely recognized.

As experience was gained with the doubly anisotropic bidomain model, it became clear that the model might be able to explain several long-standing puzzles in cardiac electrophysiology, including the mechanisms for cathodal and anodal make and break excitation,[11] as well as predict specific details of not-yet-observed phenomena, such as how a long premature pulse from a point source could induce a quatrefoil reentry pattern due to unequal dual anisotropies in myocardium.[18–22] As we see when these two predictions and their confirmation are discussed later in this chapter, there is now unequivocal evidence, at least macroscopically, that the traditional model of cardiac tissue as a nonlinear monodomain should be replaced by a nonlinear bidomain with dual anisotropies.

The peculiar distribution of tissue depolarization and hyperpolarization, as described by virtual cathodes and anodes, during and immediately after tissue excitation, raises an important question as to how these patterns interact with wave front propagation. Because these patterns are more pronounced when the intensity of the stimuli approximates that required for defibrillation, their interaction with dynamic wave fronts should have important implications in defibrillation research. Thus, there is increasing evidence that tissue anisotropy, as described by the unequal anisotropy bidomain model, determines the spread of stimulus and action currents in a manner that affects the initiation and propagation of action potentials in both the normal and the abnormal heart. It is from this perspective that we describe the evolution of our imaging system and discuss how the bidomain model and epifluorescence imaging of the cardiac transmembrane potential support new perspectives in cardiac electrophysiology.

Optical Imaging Approach

Because the bidomain responses in cardiac tissue are manifested more clearly in the transmembrane potential rather than in the extracellular potential, the optical recording technique is ideally suited to allow high-resolution observation of bidomain behavior. During the past few years, we have developed several imaging systems with different configurations specifically designed for a variety of bidomain research projects. The first system, shown in Figure 2, was a small-field, synchronous-capture epifluorescence cardiac imaging technique with wide dynamic range and high temporal and spatial resolution to image point activation patterns.[23,24] The wide dynamic range and precise timing control of the system provided us with the capability to capture synchronously a small, fractional change in the laser-induced epifluorescence proportional to transmembrane potential change. Boxcar averaging techniques in which the stimulus timing was sequentially shifted with respect to the stroboscopic illumination of the heart allowed us to achieve frame exposure times of only 0.5 ms and interframe intervals of a millisecond with a camera that had an intrinsic speed of only 7 frames per second (fps).

Subsequently, the camera system was upgraded to allow asynchronous imaging of aperiodic events such as fibrillation. The image sensor (a charged couple device [CCD] camera) was replaced by a frame-transfer CCD, which employs a double buffer technique to shorten the data trans-

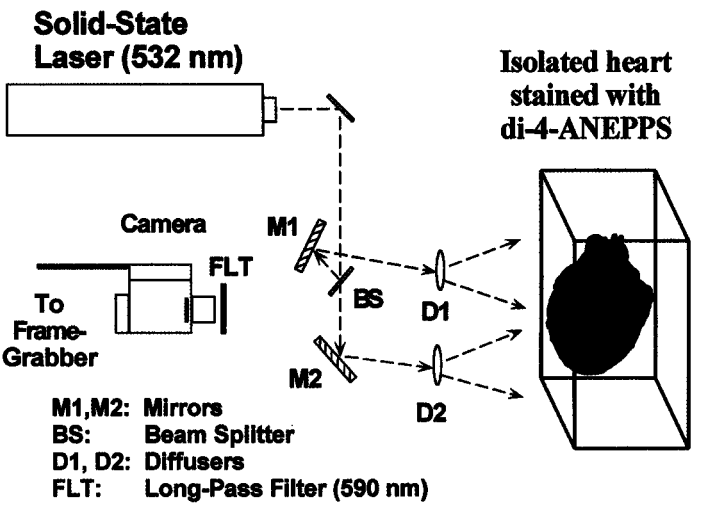

Figure 2. The first-generation synchronous imaging system developed at Vanderbilt to study cathodal and anodal make and break excitation. An acousto-optic modulator (not shown) in the laser beam allowed modulation of the laser intensity to provide submillisecond exposures of the heart to the laser illumination. Boxcar averaging techniques that involved stepwise adjustment of the interval between sequential stimuli and the laser illumination made it possible to record a sequence of 0.5-ms images separated by 1 ms with a camera that could record only 7 frames per second. Reprinted, with permission, from reference 24.

fer time. The fast frame speed led to the discovery of a quatrefoil reentry pattern[25] that had only been inferred by theoretical analyses but had never been observed in real tissue. In the meantime, a panoramic imaging technique was successfully developed to allow visualization of wave fronts on the entire heart surface,[26] as shown in Figures 3 and 4. It is now possible to measure with unprecedented detail wave front propagation on the entire heart surface. Such a capability is especially favorable for fibrillation and defibrillation studies, because the formation, maintenance, and dynamics of the reentrant patterns can be traced and measured realistically in whole heart models, not restricted to either small local areas or to only one view of the heart. We are currently completing the development of an interactive 3-dimensional wave front visualization procedure,[26,27] as well as automated, geometrical measurement of wave fronts. These are best accomplished by digitizing the 3-dimensional heart geometry using noncontact methods. The interactive visualization will allow free tilting and rotation of the computerized heart model with the animated wave fronts attached to it as texture. Such a capability will greatly facilitate geometrical tracing and measurement of the wave fronts.

The imaging system was upgraded in 1997 to a higher speed of 267 to 330 fps, with a frame resolution of 128×64 pixels.[27] This was achieved by

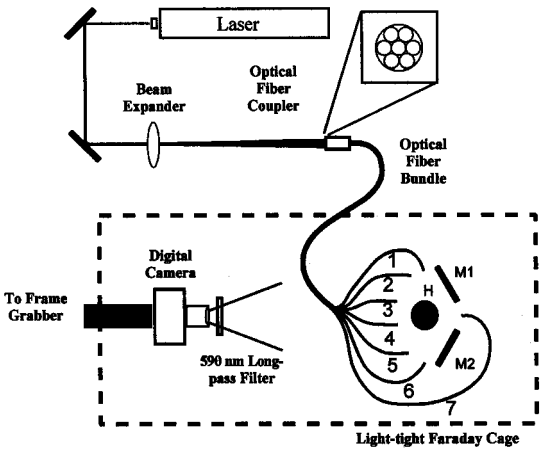

Figure 3. Schematic layout of the panoramic imaging system developed at Vanderbilt. The mirrors M1 and M2 not only allowed the camera to view the front of the heart, but also provided two other simultaneous views that included lateral and posterior portions of the heart. The seven optical fibers could be adjusted to provide uniform illumination over the entire heart.

replacing the cooled CCD camera with a faster room temperature camera, and by increasing the speed of the frame grabber and the computer. In addition, a graphic user interface panel was designed to allow fast playback of the acquired image sequences with simplified processing algorithms. More advanced image processing, including temporal/spatial filtering and analysis of electrodynamics, is performed after the experiment to improve the image quality and to extract important wave front information. Movies are produced to allow visualization of the dynamics of wave front propagation. These movies were found to be superior to frame-by-frame inspection in revealing the dynamic information due to the involvement of human visual perception. Recently, we have completed the design of camera-control software to obtain a maximum imaging speed of 1200 fps at 64×64 pixels with a 12-bit digitization.

The Role of Virtual Electrodes in Cardiac Stimulation

A surprising and unexpected result of our early bidomain simulations[10] was that during unipolar cathodal stimulation, cardiac tissue is depolarized in a dog-bone-shaped region (the virtual cathode) that lies underneath and adjacent to the cathodal electrode, and that a pair of hyperpolarized regions (virtual anodes) exist adjacent to the cathode along the directions parallel to the myocardial fibers. Until the application of high-resolution optical imaging, the complete dog-bone-shaped activation patterns had not been observed directly, despite numerous predictions from

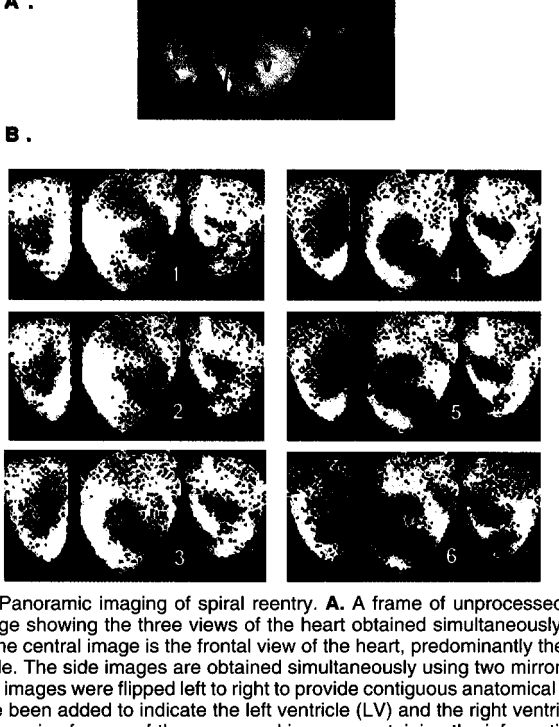

Figure 4. Panoramic imaging of spiral reentry. **A.** A frame of unprocessed fluorescence image showing the three views of the heart obtained simultaneously with the camera. The central image is the frontal view of the heart, predominantly the anterior left ventricle. The side images are obtained simultaneously using two mirrors. These side mirror images were flipped left to right to provide contiguous anatomical features. Lines have been added to indicate the left ventricle (LV) and the right ventricle (RV). **B.** Six successive frames of the processed images containing the information about V_m distribution at different times during fibrillation. The black patterns represent fully depolarized tissue. Note the evolution of the spiral wave front in the central panels and an independent reentrant pattern on the rightmost images. These frames are out of a set of 100 recorded at 67 frames per second with a 2-ms laser exposure time.

model calculations and electrode experiments that inferred its existence.[15] In 1995, three laboratories, including ours, published experimental results[23,28,29] that provided unequivocal evidence in support of the prediction that stimulation with a point electrode creates perpendicularly positioned virtual cathodes and virtual anodes, with the orientation of the patterns determined by the local muscle fiber orientation.[10] The shape of the virtual cathode and anodes was most clearly shown in our images recorded from refractory epicardial tissue of an isolated rabbit heart, as shown in Figure 5A.

We considered stimulation not only with a cathode, but also with an anode. In this case, the tissue is hyperpolarized under the anode but depolarized at regions along the fiber direction (virtual cathodes), as can be seen in Figure 5B.

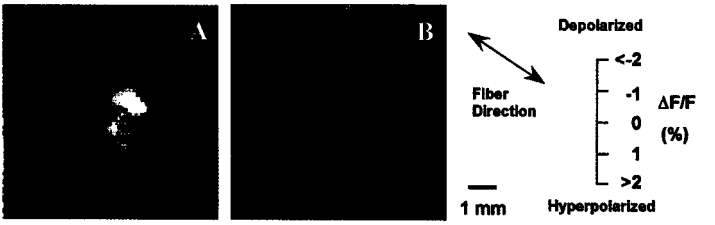

Figure 5. False-color images of the transmembrane potential associated with injection of current into refractory cardiac tissue. **A.** Image for a −10-mA, 2-ms cathodal S2 stimulus applied at a point electrode. Note the dog-bone-shaped virtual cathode (orange) and the pair of adjacent virtual anodes (blue). The fiber orientation is from lower right to upper left. The range in colors corresponds to a total fluorescence change of greater than 4%. **B.** Complementary image for a +10-mA, 2-ms anodal S2 stimulus at the same location on the heart. Note that the dog bone is now the virtual anode (blue), whereas the adjacent areas are the virtual cathodes (orange). Reprinted from reference 23, with permission from *Biophys J.*

While the virtual electrodes in Figure 5 were recorded from refractory tissue, for which there would be no propagating response, the same effects would be expected for application of a stimulus to resting cardiac tissue. Most importantly, the simultaneous existence of virtual cathodes and anodes for either a cathodal or anodal stimulus provides a mechanism for anodal stimulation: if the depolarization is strong enough, a wave front can be excited that propagates outward from the pair of virtual cathodes that are adjacent to the central, anodal dog-bone. This mechanism for anodal stimulation is called anodal make, because it occurs after the start (or make) of the stimulating pulse. The role of virtual cathodes and anodes for cathodal make and anodal make stimulation is shown schematically in Figure 6.

Theoretical models also showed that virtual electrodes play an important role in anodal break and cathodal break stimulation.[11] Anodal break and cathodal break stimulation of cardiac tissue have both been observed for decades,[30–34] but no adequate mechanism appropriate to cardiac tissue had been proposed until the bidomain studies. Break stimulation is defined as excitation that occurs upon the termination (or break) of a long stimulus pulse. With the doubly anisotropic bidomain model, the predicted mechanism of cathodal break stimulation is as follows: The strong hyperpolarization within the virtual anode removes any inactivation of the sodium channels resulting from the prolonged depolarization, and thereby renders the tissue excitable, but during the stimulus, there is no charge available by which this tissue could be stimulated. The tissue within the virtual cathode is depolarized throughout the duration of the pulse and remains unexcitable after the end of the stimulus for an interval approximately equal to the refractory period. However, upon the break of the stimulus, the positive charge that has been localized inside the cells within the depolarized virtual cathode can now diffuse into the hyperpolarized tissue within the virtual anode and excite it. Figure 6D shows how the activation wave fronts (yellow lines) will propagate away from the pair of virtual anodes adjacent

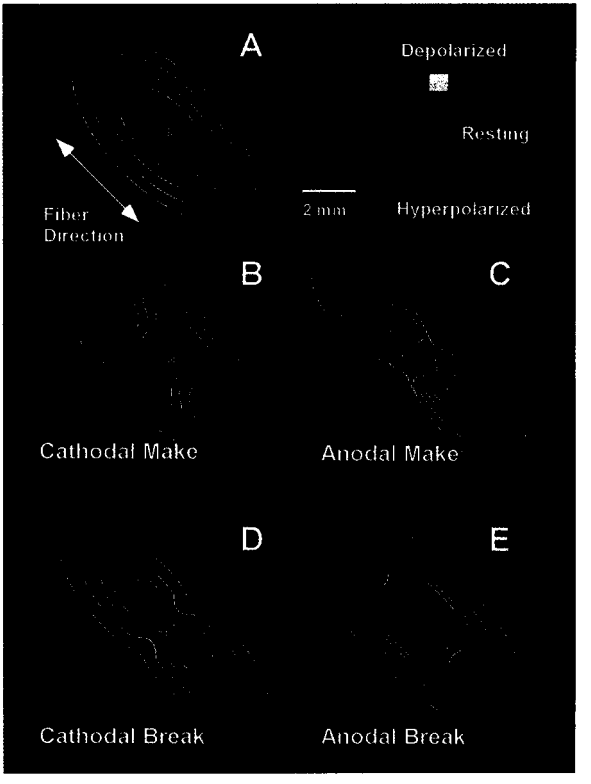

Figure 6. Schematic representation of the theoretical predictions of action potential propagation for point stimulation of cardiac tissue (based on references 9 through 11). **A.** Cathodal make stimulation in an equal anisotropy model. An elliptical region of tissue would be directly depolarized (orange) by a strong point stimulus (black dot) and would act as a virtual cathode. An elliptical action potential wave front (yellow lines separated by 2 ms) would propagate away from the edge of the virtual cathode. **B.** Cathodal make stimulation in a model with differing anisotropic conductivities for the intracellular and extracellular spaces. The virtual cathode is yellow to orange and the virtual anode is blue. The resulting propagating wave front would initially have the transverse dog-bone shape, but because of the greater longitudinal conduction velocity, the wave front would become elliptical by the time it was 5 mm from the stimulus electrode. **C.** The same model as in B, but for anodal make stimulation. A pair of action potential wave fronts propagating outwardly from the virtual cathodes (orange) merge and form an elliptical wave front within 1 cm of the stimulus electrode. **D.** The same model for cathodal break stimulation. Early activation occurs from the virtual anodes (blue) along the fiber direction. **E.** Anodal break stimulation, in which initial activation progresses transverse to the fibers from the dog-bone-shaped virtual anode (blue). Reprinted from reference 23, with permission from *Biophys J.*

to the dog-bone-shaped virtual cathode, but will be blocked initially from propagating through the refractory virtual cathode.

A similar mechanism was predicted to underlie anodal break stimulation, with the exception that a smaller amount of charge is stored within the pair of virtual cathodes and the nonlinearity of the membrane conductance may play a larger role in the stimulation process. This process is shown in Figure 6E, wherein the anodal break activation again propagates away from the virtual anode, which in this case is dog-bone shaped, and is delayed by the pair of adjacent virtual anodes.

Using our synchronous fluorescence imaging system, we verified all four mechanisms of unipolar stimulation: cathodal make, anodal make, cathodal break, and anodal break.[11] As shown in the leftmost column of Figure 7, we were able to observe the initial activation patterns of all four

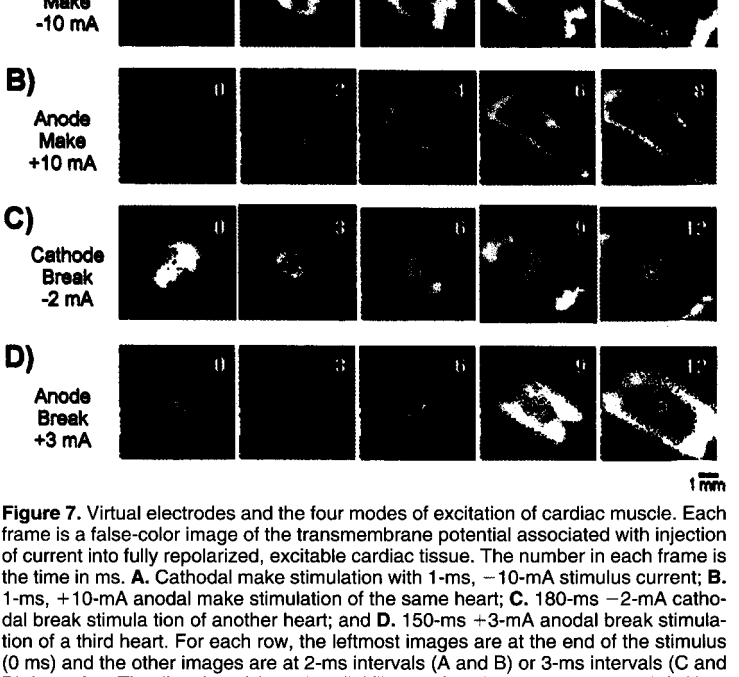

Figure 7. Virtual electrodes and the four modes of excitation of cardiac muscle. Each frame is a false-color image of the transmembrane potential associated with injection of current into fully repolarized, excitable cardiac tissue. The number in each frame is the time in ms. **A.** Cathodal make stimulation with 1-ms, −10-mA stimulus current; **B.** 1-ms, +10-mA anodal make stimulation of the same heart; **C.** 180-ms −2-mA cathodal break stimula tion of another heart; and **D.** 150-ms +3-mA anodal break stimulation of a third heart. For each row, the leftmost images are at the end of the stimulus (0 ms) and the other images are at 2-ms intervals (A and B) or 3-ms intervals (C and D) thereafter. The direction of the epicardial fibers is from lower right to upper left. Note that in both cathodal make and anodal make excitation, the early propagating wave fronts in the 2-ms and 4-ms frames are seen to originate from the orange virtual cathodes in the 0-ms frame; in break excitation, the early propagating activity in the 3-ms and 6-ms frames originates from the hyperpolarized virtual anodes in the 0-ms frame. Reprinted from reference 23, with permission from *Biophys J.*

different modes of cardiac stimulation, as well as the subsequent outwardly propagating wave fronts. The agreement with the theoretical predictions (Fig. 6) is remarkable.

The experimental observation of these phenomena would have been difficult using electrical mapping techniques that record the extracellular signals, because the early activation patterns appear only in the transmembrane potential distribution,[10] and these activation patterns are essentially embedded in the electrical stimulus artifact. Thus, optical techniques provided, for the first time, the ability to image directly and with submillimeter spatial resolution both the virtual anodes and cathodes during activation and the subsequent propagating wave fronts. Our results clearly demonstrated that current injection into the extracellular space of tissue with unequal anisotropies simultaneously produces distinct depolarized and hyperpolarized regions of transmembrane potential that are the mechanism by which anodal make and anodal break excitation occurs. This study also demonstrated that the differing anisotropic conductivities of the intra- and extracellular spaces are not just a biophysical curiosity but play a significant role in the stimulation of the heart with strong electrical current.

Discovery of Quatrefoil Reentry

Single spiral wave rotors with circular movement, and two opposing rotors with a figure-of-8 reentrant pathway are basic patterns of electrically induced reentry in normal cardiac muscle that provide the fundamental elements for understanding and treatment planning of many cardiac arrhythmias. In contrast to anatomical reentry that arises from an anatomical obstacle or inhomogeneity about which the reentrant excitation propagates, both of these functional reentry patterns can be produced in anatomically homogenous tissue solely by the interaction between a spatial gradient in stimulus strength and another spatial gradient in excitability. As a result, the reentrant activation propagates around a phase singularity, i.e., a region of tissue whose electrical phase is indeterminate, with the spiral wave exhibiting a single singularity and a wave front that extends from this singularity to the edge of the active tissue, and figure-of-8 reentry having a pair of singularities that define the ends of a wave front.

Theoretical studies based on the dual anisotropies in cardiac tissue suggested the existence of an unusual 4-loop reentry.[18–22] Using numerical simulations, Roth and Saypol[20–22] found that when the pacing (S1) and the premature (S2) stimuli were delivered at the same site on the tissue, the hyperpolarization at the virtual anode shortened the refractory period of the S1 wave front parallel to the fibers, and the depolarization at the virtual cathode lengthened the refractory period of the S1 wave front perpendicular to the fibers. Thus, a wave front initiated by the S2 stimulus could propagate parallel to the fibers, but was blocked perpendicular to them. This "arc of functional conduction block" would lead to a fourfold symmetrical reentrant pattern in their computer model, shown in Figure 8.

Similar to other functional reentry patterns, the reentry is established by the interaction of a spatial gradient in excitability following the S1 stimulus with a differing spatial gradient in the strength of the S2 stimulus.

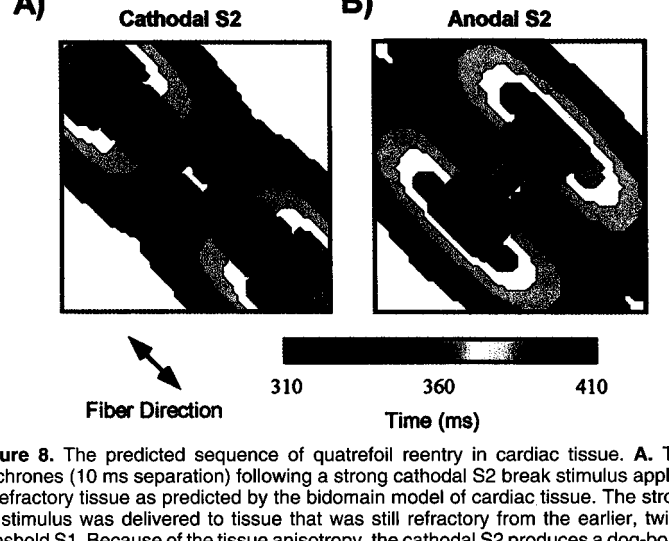

Figure 8. The predicted sequence of quatrefoil reentry in cardiac tissue. **A.** The isochrones (10 ms separation) following a strong cathodal S2 break stimulus applied to refractory tissue as predicted by the bidomain model of cardiac tissue. The strong S2 stimulus was delivered to tissue that was still refractory from the earlier, twice-threshold S1. Because of the tissue anisotropy, the cathodal S2 produces a dog-bone-shaped virtual cathode region that maintains the tissue depolarization and refractoriness. The adjacent anodal regions on either side of the dog-bone are hyperpolarized by S2, which returns the tissue to excitability. At the end of S2, charge flows from the cathodal region into the anodal ones, so that activation propagates along the fiber axis but is blocked from spreading transversely. Subsequently, the wave front propagates around the region that was directly polarized during the S2 stimulus, so that the S2 wave fronts finally reenter toward the electrode from both sides, collide near the electrode, and then launch another wave front that again moves along the fiber direction. **B.** The isochrones predicted for an anodal break S2. Courtesy of Bradley Roth.

Winfree[19] has described this in terms of the critical point hypothesis, in which phase singularities, about which the reentrant wave front propagates, are created at the intersection of the excitability contour T* and the stimulus threshold contour S*. In spiral wave reentry, crossed-field stimulation by a pair of orthogonal line electrodes produces orthogonal T* and S* that cross at the point that defines the fixed end of a spiral wave; figure-of-8 reentry occurs when the T* generated by a planar S1 wave front crosses a circular S* from a point stimulus, producing a pair of singularities that define the ends of a single wave front. Quatrefoil reentry is unique in that it can be produced by sequential stimulation by a single electrode: a nearly elliptical T* from S1 is cut four times by the dog-bone-shaped S* of a strong S2 delivered at the same stimulus site. Consequently, there are four phase singularities that define the ends of a pair of synchronized wave fronts.

Using our frame-transfer CCD camera system, we performed high-speed imaging to investigate the induction mechanism of such a peculiar reentrant pattern. In 16 isolated, Langendorff-perfused rabbit hearts, high-speed optical imaging at 133 or 267 fps allowed us to observe the induced response with a unipolar point electrode. Delivering long stimuli during

the vulnerable phase created the novel quatrefoil-shaped reentry pattern consisting of two pairs of opposing rotors. Successful induction occurred in a narrow range of coupling intervals. A dog-bone pattern of virtual electrodes was established during the premature stimulus (Fig. 9A). Wave fronts that were launched began to propagate from the virtual anodes immediately after the termination of S2. The alternating blocking and conducting effects of the virtual electrodes, as well as the boundary between virtual cathode and virtual anode, provided the necessary substrate for quatrefoil reentry. As predicted by the theory, the direction of propagation of the reentrant spiral wave fronts reversed with a reversal in S2 polarity (not shown). Because of interference by secondary wave fronts propagat-

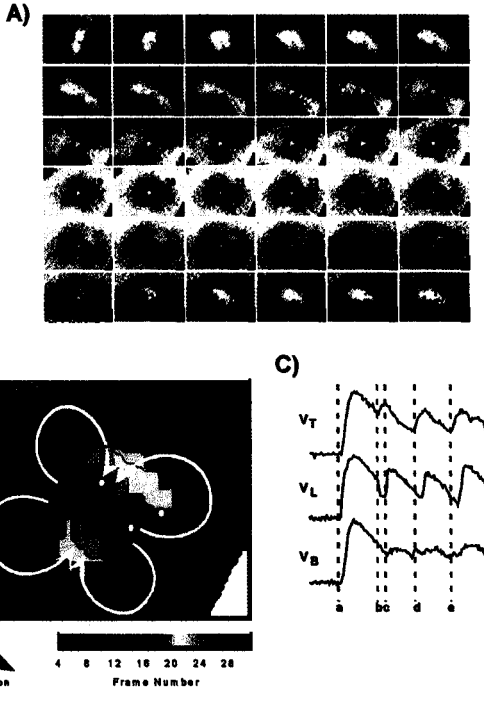

Figure 9. A. Dye-fluorescence images of the transmembrane potential of an isolated rabbit heart as a function of space and time during cathodally induced quatrefoil reentry. A cathodal S2 stimulus (−20 mA, 20 ms) is applied at the center of the tissue; the stimulus ends after frame 1. Adjacent frames are separated in time by 3.8 ms, and show a 20×13.5-mm^2 area of tissue. The arrow indicates the fiber direction. **B.** Pseudo-color isochronal map showing the position of the activation wave front at subsequent times after the end of the S2 stimulus. **C.** The transmembrane potential as a function of time, at the three different locations marked T, L, and B. The vertical dotted line a is the time of the last S1 stimulus, b and c are the start and end of the S2 stimulus, and d and e are start times of subsequent depolarizations in the VT trace. The V_B trace shows that the B recording site in panel B is within or near the region of functional block.

ing back into the region of the reentrant pattern, quatrefoil reentries were not sustained and lasted between one and four complete cycles.

One of the key findings of our studies of quatrefoil reentry is that for strong shocks we can clearly distinguish between cathodal make or anodal make activation, for which the wave front propagates away from the depolarized virtual cathode, and cathodal break or anodal break activation, for which activation propagates from the hyperpolarized virtual anode. Activation of cardiac tissue by the break mode of stimulation may prove to be an additional new mechanism for defibrillation.

Tissue-Medium Interface

The role of the tissue surrounding the heart is important in transthoracic defibrillation, in that the distribution of defibrillation currents and the fraction of currents that actually enter the heart are determined by the conductivity of the skin, the thoracic muscles and ribs, the lungs, the mediastinum, and the great vessels. The effects of the extracardiac tissues and great vessels on intracardiac defibrillation, such as with an implantable defibrillator, is not well known. Studies of internal defibrillation are conducted on intact humans either during transthoracic surgery or in the catheterization lab, on intact dogs or dogs with exposed hearts supported in a pericardial cradle, and on isolated rabbit or dog hearts in air or in a conducting bath. In each of these preparations, the heart is located in a different conducting environment, and if the surrounding environment has any effect on cardiac defibrillation, then there could be substantial differences between studies conducted with different conductor configurations. An example of the effect of extracardiac conductivity is shown in Figure 10,[35] which demonstrates the modeling results of tissue response from an endocardial shock. Although the endocardial response appears to be the same, the epicardium shows different activation patterns due to different tissue-medium interface conditions.

In a monodomain model of the heart, the heart-tissue interface serves as a boundary between two regions of differing conductivity, and the primary effect of the interface is to alter the direction of the electrical field and thereby bend the lines followed by the electrical current. In the bidomain model, the situation is substantially more complex. For example, current flowing in a passive monodomain, such as the blood, crosses into the bidomain by the extracellular space, and then proceeds to redistribute itself between the intra- and extracellular spaces in accordance with the length constant of the tissue. The transmembrane potential reflects this redistribution of current and shows the effect predominately within a length constant of the surface.

Although the bidomain boundary effects have been the subjects of some theoretical debate,[36] there have been few direct observations of boundary effects. One of the clearest demonstrations involves comparison of the epicardial transmembrane potential during application of intracardiac defibrillation-strength shocks. Figure 11A shows tissue response from an endocardial anodal shock with an isolated, Langendorff-perfused rabbit heart pressed against the frontal glass window of the bath. The activation

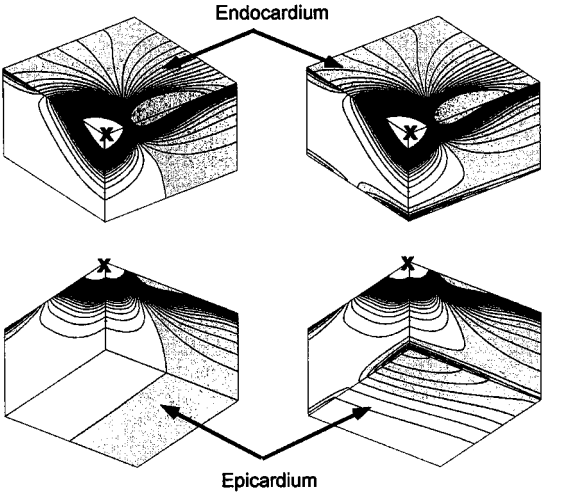

Figure 10. Model predictions of the transmembrane potential during intracardiac defibrillation in a slab of cardiac tissue that is 5 mm × 5 mm × 3 mm thick. Only one quarter of the tissue is shown. *Left:* Endocardial (upper) and epicardial (lower) views of the potential distribution when the epicardial surface is bounded by an insulator. The shaded regions have a negative transmembrane potential change due to the shock. Contours are every 300 mV; contours above 20 V and below −7 V have been omitted. *Right:* The same views when the epicardial surface is bounded by a conducting bath. Note the two endocardial distributions are similar but there is a pronounced rotation of the potential distribution and the zero-volt line between the two boundary conditions. Reprinted from reference 35, with permission of *IEEE Trans Biomed Eng.*

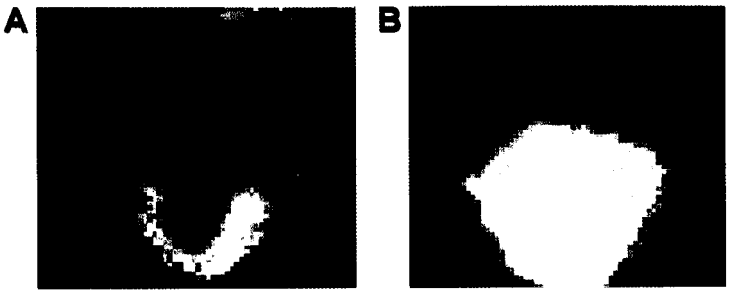

Figure 11. The dye fluorescence image of the epicardial surface of an isolated rabbit heart during an intracardiac defibrillation-strength anodal shock. **A.** The heart is pressed against a glass plate to produce a horseshoe-shaped depolarized region (yellow) surrounding a hyperpolarized one (blue). **B.** The heart is suspended freely in the bath, and only depolarization is evident on the epicardium.

pattern shows a horseshoe-shaped depolarized region surrounding a negatively polarized region. Such an epicardial observation of bipolar response from endocardial shocks is consistent with the result obtained in the right ventricle by Efimov et al.[37] However, when the heart was suspended in the bath without being pressed against the frontal window, the tissue response did not show such a horseshoe pattern (Fig. 11B), and the negative polarization cannot be observed from optical recordings on the epicardium.

The difference between these two epicardial responses could be the result of 1) changes in the propagation of direct activation during the shock, or 2) differences between the heart-medium interface through the action of pressing the heart against the frontal window. Using high-speed imaging at 1200 fps with a frame interval of 0.8 ms, we observed the progression of tissue response during the shock. The results showed that the negative polarization was not detectable with our instrumentation when the heart was freely suspended in the bath. Therefore, we conclude that the high impedance created by the heart-plate interface is responsible for the bipolar response as shown in Figure 11A, in that the plate serves as a no-current boundary and prevents current from leaving the bidomain at the epicardium and from producing a large transmembrane potential change at the monodomain/bidomain interface.

For the first time, the ability to observe regions of depolarization and hyperpolarization during the shock and to identify these in terms of virtual anodes and cathodes had made possible the detailed examination of the mechanisms by which a defibrillation shock alters the state of cardiac tissue over large regions of the heart. Studies by the group of Efimov[37,38] as well as those studies reported in this chapter demonstrate that the transmembrane potential distribution on the epicardial surface depends upon whether the heart is hanging free in a bath or pressed up against an insulating window. Mathematical modeling by Latimer and Roth[35] confirms that the epicardial potential distribution is altered significantly between a surrounding material of air or saline. All of these observations suggest that interpretations of transmembrane potentials on the epicardial surface during defibrillation are strongly affected by the surrounding environment. We conclude from these studies that investigators studying defibrillation mechanisms must be aware that the transmembrane potential distributions on the epicardial surface depend upon the electrical conductivity of the surrounding medium.

The Role of the Bidomain Model in Cardiac Defibrillation

In the past few decades, a trend in defibrillation research has been established toward the understanding of mechanistic shock action. Chronologically, the proposed defibrillation mechanisms include total extinction,[39] critical mass,[40,41] upper limit of vulnerability (ULV),[42] and synchronization of repolarization.[43] Other defibrillation mechanisms, including more speculative ones such as perturbation of chaotic systems,[44] generated a lot of interest, and experimental results have been gathered to support the chaotic nature of ventricular fibrillation.[45,46]

The relationship between defibrillation energy or voltage or current and the likelihood of success has been found experimentally to be well described by a sigmoid-shaped curve, reflecting a probabilistic function.[47] Actual defibrillation thresholds (DFTs) must be determined experimentally, and even mathematical models of defibrillation current distributions require empirical calibration.[48] Surprisingly, there is no theory or mathematical model that provides a first-principles connection between the vast knowledge of cellular cardiac electrophysiolo gy and the growing understanding of fibrillation and defibrillation. Today, there are no models that can predict, from a description of ion channel kinetics, the response of a fibrillating heart to a defibrillation shock. The role of tissue anisotropy in the distribution of defibrillation currents is unknown.

It is no coincidence that the progress in defibrillation research is tightly coupled to the capability of the research instrumentation, especially the exponential increase over the years in the number of recording sites on the heart. It is through the advances in instrumentation that many different levels of defibrillation mechanisms can be pursued.[49] By recording simultaneously from a large number of sites, more global information, such as reentrant conduction pathways, location of the ectopic focus, or wave front curvature, can be investigated. The hypotheses of total extinction and critical mass were proposed when only a small number of recording sites were available. Such views have led to the argument over continued versus regenerated fibrillation wave fronts.[50,51] In contrast, the ULV hypothesis has been studied extensively by the group of Ideker and Chen,[42,49,50] with an electrical mapping system of more than 200 recording sites. This hypothesis has significant clinical implications because a correlation between ULV and DFT has been suggested.[42] However, the ULV hypothesis has been reevaluated recently, in theory and in experiment,[52,53] as a result of rare experimental observations of critical point formation resulting from delivered shocks, and also due to the dynamic variation of isocontours during the shock. The ability to record the transmembrane potential using optical recording techniques has led to a recent hypothesis of synchronization of repolarization.[43]

Of all of the questions presented by cardiac defibrillation, the most fundamental relates to the interaction between the electrical field of the shock and the transmembrane potential of individual cardiac cells. It is well recognized that the myocardial syncytium has cablelike properties, including an exponential drop in transmembrane potential with distance from an extracellular electrode, described by a length constant of 1 or 2 mm. Hence, during a defibrillation shock, one might expect that cells only within a few length constants of the electrodes would experience appreciable changes to their transmembrane potential, and that the bulk of the heart would be unaffected. However, it is clear that a sufficiently strong defibrillation shock, delivered by some combination of transthoracic, epicardial, or intracavitary electrodes, can render virtually all of the heart transiently unexcitable.

Obviously, changes in transmembrane potential are required to render cardiac tissue unexcitable, but a uniform cable can carry large amounts of current, appropriately distributed between the intracellular and extracellular spaces, without requiring transmembrane potential differences

beyond several length constants from the electrodes. One hypothesis to address this problem was advanced 10 years ago: with the sawtooth mechanism, the discrete cell-to-cell resistance at the gap junctions causes each cell to be depolarized and hyperpolarized on opposite ends.[54,55] If the sawtooth has sufficient amplitude, one end of each cell would be depolarized above threshold, and the resulting sodium influx would then depolarize the entire cell. This could provide a possible explanation of how a shock can activate a large volume of tissue. Despite its theoretical plausibility and observation of the phenomena in a single, isolated myocyte[56,57] and a single strand of myocytes,[58] the search in real tissue or in wider cultured strands for this specific sawtooth excitation has been unsuccessful,[59,60] apparently because the staggering of adjacent myocardial cells provides shunt pathways across the high-resistance cell junctions, thereby attenuating the sawtooth amplitude.

An alternative bidomain mechanism for the interaction of defibrillation shocks with bulk myocardium was suggested by Trayanova and colleagues[61]: the curvature of the cardiac fibers and the un equal anisotropy ratios cause depolarization and hyperpolarization throughout the heart, in that as the applied stimulating currents transverse the heart, they encounter fibers at different orientations, which would induce a redistribution of current between the intracellular and extracellular spaces and a concomitant change in the transmembrane potential. Their analysis also predicted that the transmembrane potential at the heart surface is quite different from the transmembrane potential below the surface. The differences may be so large that the surface may be depolarized while the bulk of the tissue is hyperpolarized.

Another bidomain mechanism has been proposed to explain the defibrillation of bulk myocardium. Under the syncytial heterogeneity hypothesis,[62] localized heterogeneities in the cellular volume fraction (the ratio of intracellular to extracellular space in a given element of myocardial tissue) at the level of a few percent could lead to current redistributions that are sufficient to depolarize the tissue. This hypothesis can be generalized to include localized heterogeneities of any number of bidomain parameters, or even millimeter-scale changes in tissue connectivity or conductivity. Thus, it appears that the bidomain model and the underlying tissue anisotropy may hold the answer to the fundamental questions of how strong shocks can inactivate most of the heart.

As a first step toward quantifying shock-tissue interactions during defibrillation, we have used optical imaging of the epicardial transmembrane potential V_m during far-field stimulation.[63] Langendorff-perfused, di-4-ANEPPS-stained, isolated rabbit hearts with atria excised were immersed in a $10 \times 10 \times 15$ cm^3 bath of Tyrode's solution. Following 20 right ventricular pacing pulses at a constant cycle length of 500 ms, a diastolic 1-ms S2 was delivered to plate electrodes at the ends of the bath to produce horizontal shock fields of ± 3.3, ± 6.7, or ± 10 V/cm. High-speed optical imaging at 322 fps measured V_m changes during and after S2. The heart axis was at either 0°, 45°, or 90° to the vertical. The prompt response of V_m was recorded in the frame taken during S2. To detect shock-induced asymmetries in V_m, we calculated the x and y components (p_x and p_y) of the dipole moment of the V_m image by integrating the prompt-response image intensity weighted by the x or y distance from the center of a pre-S2 image. Figure 12 shows the

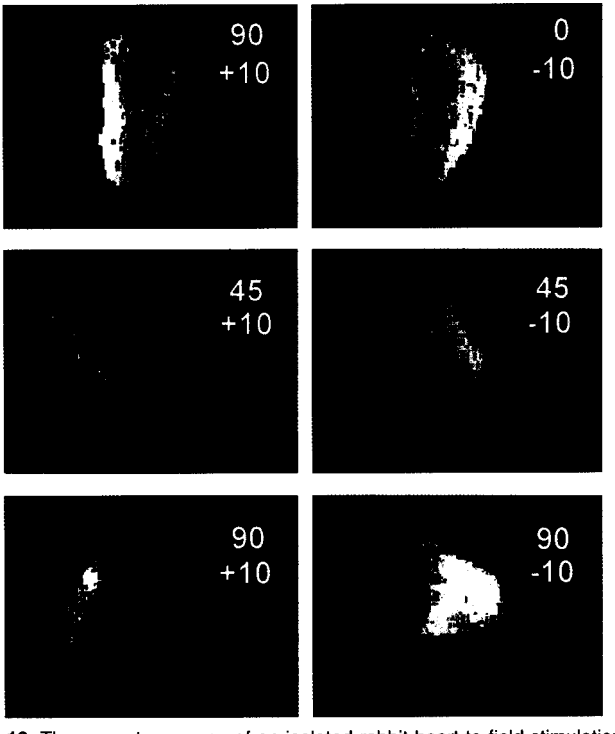

Figure 12. The prompt response of an isolated rabbit heart to field stimulation by a horizontal electrical field at three different angles and shock polarities (±10 V/cm). Red/yellow is depolarization. For 90°, +10 V/cm, the valve ring may block the field. Otherwise, the pattern is clearly determined by the orientation and sign of the field and not the orientation of the heart, consistent with the monodomain/bidomain boundary between the surrounding bath and the heart.

prompt responses of shocks delivered horizontally with the heart at three angles. Spherical and ellipsoidal models of cardiac shock response using a bidomain with unequal intracellular and extracellular anisotropy ratios and fiber curvature predict that the dominant epicardial effect arises from the monodomain/bidomain interface, which to first order is independent of the orientation of the underlying fibers. As a result, the cardiac surface facing the cathodal electrode would exhibit depolarization while the surface facing the anode would hyperpolarize.[61,64] If macroscopic or cellular conductivity discontinuities play the dominant role in defibrillation, prompt depolarization would be expected on both sides of the heart. Our data show that p_x is determined by shock strength and polarity; our data are not yet adequate to ascertain whether we can detect secondary, fiber orientation ef-

fects, in the form of a p_y dipole moment or curvature of the isopotential line between the depolarized and hyperpolarized regions of the epicardium. We are continuing with these experiments, and are devising experimental configurations for which the boundary effects should be smaller than those due to bidomain anisotropies or heterogeneities.

Conclusions

Over the past decade, a variety of linear and nonlinear bidomain models have been developed.[11,12,14–17,23,65,66] New instrumentation and experimental techniques have been devised to test quantitative predictions by these models, and we have conducted a series of in vitro experiments to provide qualitative and quantitative tests of most of the specific predictions of the bidomain model. The results present convincing evidence that at the spatial scale of 1 mm and larger the bidomain model accurately describes the electrical behavior of cardiac tissue, particularly its response to strong electrical shocks. The bidomain model with unequal electrical anisotropies has been used to make a number of surprising and nonintuitive predictions that were not anticipated by earlier models, such as the existence and shape of virtual cathodes and anodes, which were subsequently confirmed experimentally. The unequal anisotropy bidomain model provides the first explanation of how cathodal and anodal make and break stimuli induce propagating activation. The experimental confirmation of quatrefoil reentry is the capstone of these predictions.

The bidomain model has led to the replacement, during excitation from a point source of strong currents, of the traditional concept of an elliptical excitation wave front with a cloverleaf, or dog-bone, excitation pattern.[11,23] Furthermore, the shock effects from either far-field shock electrodes, epicardial patches, or internal coil electrodes have been shown to be consistent with bidomain predictions.[37,63,67–69] It is important to emphasize that the phenomena that validate the bidomain model all result from differences in the electrical anisotropy of the electrical conductivities of the intracellular and extracellular spaces. Because of these differences, the spatial distribution of stimulus currents will differ between the two spaces, which in turn leads to previously unexpected transmembrane potential distributions. These phenomena in turn have led to the revision of several historical concepts in cardiac electrophysiology, including defibrillation mechanisms. A representative case is the reevaluation of the critical point hypothesis,[18,70] which was based on simple excitation and repolarization gradients to determine the intersecting singularity points. The complex rather than simple pattern of excitation gradients will make it necessary to review this important hypothesis in fibrillation and defibrillation theory.[52]

Given the recent demonstrations of the cardiac bidomain response and the growing acceptance of the bidomain concept in the cardiac electrophysiology community, it is worthwhile to contemplate the future contributions that such a model may offer. Historically, the electrical behavior of the membrane of isolated cardiac myocytes has been studied using patch-clamp recordings and carefully designed current and voltage protocols. The

immediate response of cardiac tissue to electrical stimulation, as occurs during pacing and defibrillation, has been studied with micropipettes that measure the transmembrane potential, V_m, of a single cardiac cell, or with dye/fluorescence techniques that record from a number of adjacent cells, or with macroscopic electrodes that are placed within the myocardium or on the epicardial, endocardial, or torso surfaces. The models used to explain the resulting data have a similar span in spatial scales and describe, for example, the kinetics of single ion channels or the movement of activation wave fronts through the heart. The challenge facing defibrillation research is to couple channel-scale and cellular-scale observations to those of the whole heart, recognizing that in fibrillation all scales are active: from the single channel to the macroscopic geometry of the reentry pathways.

Thus, a detailed understanding of the propagation of electrical activity through ventricular myocardium requires a knowledge of both the electrical behavior of an individual cardiac cell and the role of the cardiac syncytium that couples together the 4 billion cells that form the ventricles. A similar range of scales occurs in atrial fibrillation. Over the past decade, patch-clamp techniques, coupled with molecular biology, have been providing an increasingly clear picture of ion channel structure and the role of specific ion channels in the cardiac action potential. Progress has been slower in combining this knowledge with models of myocardial tissue, primarily because of the formidable computational challenge imposed by the requirements for 10-μm spatial discretiza tion and 5-μs time steps in a simulated block of myocardium, no less the entire heart. At present, models that support active propagation of wave fronts are discretized at the scale of a millimeter, and hence cannot include cellular level effects such as the explicit role of intercellular discontinuities and intracellular gradients in voltage or channel density. Although the spatial resolution and geometric and physiological complexity of models is continually increasing, it is unlikely that a single model will be able to span between the ion channel and the whole heart. Given the present impossibility of such a calculation, *the bidomain model offers great promise as a physiologically realistic intermediate step to link the submicron spatial scale associated with molecular electrophysiology to the 10-cm spatial scale of macroscopic electrical behavior of the intact heart.* Toward this end, the bidomain model has already far exceeded the ability of other models to make quantitative predictions regarding cardiac electrical activity that subsequently have been verified experimentally. The coupling of realistic bidomain models of the entire heart with detailed electrophysiological models of the cardiac membrane promises to be a fruitful area of cardiac research.

From this perspective, there are a number of questions that remain to be answered, about the bidomain model and about cardiac electrophysiology. At issue are concerns such as how best to describe the actual cardiac syncytium at all spatial scales, how spatial variations in electrical anisotropies, other bidomain parameters, and tissue macrostructure affect propagation of depolarization and the spread of repolarization, and how myocardium responds to external electri cal stimuli of differing time courses. The clinical cardiac literature is replete with observations of electrophysiological phenomena that have defied theoretical explanation, such as the strength-interval characteristics of two sequential stimuli and

the differences in threshold for monophasic and biphasic stimuli. Other areas of interest include the exact angular dependence upon conduction velocity, wave front curvature during collisions, and the effect of the conductivity of the medium surrounding the heart on both propagating action potentials and defibrillation shock distributions. Some phenomena, such as the directional dependence of the rate of rise of V_m, have been addressed with models that may be unnecessarily complicated or whose wider impli cations are not fully understood, such as cardiac models with large numbers of discrete cells. As the role of individual ion channels is described in finer and finer detail, the severity of the gap between our understanding of the molecular electrophysiology of the heart and our knowledge of how the $\approx 10^9$ cardiac cells interact to form the heart is becoming more pronounced. Reentrant phenomena that exist at spatial scales of 1 mm to 1 cm will undoubtedly be governed by both ion channel kinetics and the nature of the 3-dimensional cardiac cable, which in some cases must include local heterogeneities. Addressing these questions and others will require further refinement of the advanced optical, electrical, and magnetic recording techniques developed so far, and may require extension of the bidomain model to include the effects of regional heterogeneities and discontinuities in tissue conductivity.

References

1. Corbin LV, Scher AM. The canine heart as an electrocardiographic generator. Dependence on cardiac cell orientation. *Circ Res* 1977;41:58–67.
2. Colli-Franzone P, Guerri L, Viganotti C, et al. Potential fields generated by oblique dipole layers modeling excitation wavefronts in the anisotropic myocardium. Comparison with potential fields elicited by paced dog hearts in a volume conductor. *Circ Res* 1982;51:330–346.
3. Muler AL, Markin VS. Electrical properties of anisotropic neuromuscular syncytia. I. Distribution of the electrotonic potential. *Biofizika* 1977;22:307–312.
4. Muler AL, Markin VS. Electrical properties of anisotropic neuromuscular syncytia. II. Distribution of a flat front of excitation. *Biofizika* 1977;22:518–522.
5. Muler AL, Markin VS. Electrical properties of anisotropic neuromuscular syncytia. III. Steady state of the front of excitation. *Biofizika* 1977;22:671–675.
6. Tung L. *A Bidomain Model for Describing Ischemic Myocardial DC Potentials* [PhD dissertation]. Cambridge, MA: MIT; 1978.
7. Geselowitz D, Miller W. A bidomain model for anisotropic cardiac muscle. *J Biomed Eng* 1983;11:191–206.
8. Plonsey R, Barr RC. Current flow patterns in two-dimensional anisotropic bisyncytia with normal and extreme conductivities. *Biophys J* 1984;45:557–571.
9. Roth B, Wikswo J Jr. A bidomain model for the extracellular potential and magnetic field of cardiac tissue. *IEEE Trans Biomed Eng* 1986;33:467–469.
10. Sepulveda NG, Roth BJ, Wikswo JP Jr. Current injection into a two-dimensional anisotropic bidomain. *Biophys J* 1989;55:987–999.
11. Roth BJ. A mathematical model of make and break electrical stimulation of cardiac tissue by a unipolar anode or cathode. *IEEE Trans Biomed Eng* 1995;42:1174–1184.
12. Sepulveda NG, Wikswo JP Jr. Electric and magnetic fields from two-dimensional anisotropic bisyncytia. *Biophys J* 1987;51:557–568.
13. Roth BJ. Electrical conductivity values used with the bidomain model of cardiac tissue. *IEEE Trans Biomed Eng* 1997;44:326–328.

14. Staton DJ, Friedman RN, Wikswo JP Jr. High resolution SQUID imaging of octupolar currents in anisotropic cardiac tissue. *IEEE Trans Appl Superconduct* 1993;3:1934–1936.
15. Wikswo JP Jr, Wisialowski TA, Altemeier WA, et al. Virtual cathode effects during stimulation of cardiac muscle: Two-dimensional in vivo experiments. *Circ Res* 1991;68:513–530.
16. Roth BJ, Wikswo JP Jr. Electrical stimulation of cardiac tissue: A bidomain model with active membrane properties. *IEEE Trans Biomed Eng* 1994;41:232–240.
17. Turgeon J, Wisialowski TA, Wong W, et al. Suppression of longitudinal versus transverse conduction by sodium channel block. Effects of sodium bolus. *Circulation* 1992;85:2221–2226.
18. Winfree AT. Electrical instability in cardiac muscle: Phase singularities and rotors. *J Theor Biol* 1989;138:353–405.
19. Winfree AT. Ventricular reentry in three dimensions. In Zipes DP, Jalife J (eds): *Cardiac Electrophysiology: From Cell to Bedside*. Philadelphia: W.B. Saunders Co.; 1990:224–234.
20. Roth BJ, Saypol JM. The formation of a reentrant action potential wave front in tissue with unequal anisotropy ratios. *Int J Bifur Chaos* 1991;1:927–928.
21. Saypol JM, Roth BJ. A mechanism for anisotropic reentry in cardiac muscle. *J Cardiovasc Electrophysiol* 1992;3:558–566.
22. Roth BJ. Nonsustained reentry following successive stimulation of cardiac tissue through a unipolar electrode. *J Cardiovasc Electrophysiol* 1997;8:768–778.
23. Wikswo JP Jr, Lin S-F, Abbas RA. Virtual electrodes in cardiac tissue: A common mechanism for anodal and cathodal stimulation. *Biophys J* 1995;69:2195–2210.
24. Lin S-F, Abbas RA, Wikswo JP Jr. High-resolution high-speed synchronous epifluorescence imaging of cardiac activation. *Rev Sci Instrum* 1997; 68:213–217.
25. Lin S-F, Roth BJ, Echt DS, Wikswo JP Jr. Complex dynamics following unipolar stimulation during the vulnerable phase. *Circulation* 1996;94:I714.
26. Lin S-F, Echt DS, Wikswo JP Jr. Panoramic whole-heart optical mapping of ventricular fibrillation. *Circulation* 1996;94:I48.
27. Lin S-F, Wikswo JP Jr. Panoramic optical imaging of transmembrane potential propagation in isolated heart. *J Biomed Opt* 1999;4:200–207.
28. Neunlist M, Tung L. Spatial distribution of cardiac transmembrane potentials around an extracellular electrode: Dependence on fiber orientation. *Biophys J* 1995;68:2310–2322.
29. Knisley SB. Transmembrane voltage changes during unipolar stimulation of rabbit ventricle. *Circ Res* 1995;77:1229–1239.
30. Brooks C, Hoffman BF, Suckling EE. *Excitability of the Heart*. New York: Grune and Stratton; 1955.
31. Dekker E. Direct current make and break thresholds for pacemaker electrodes on the canine ventricle. *Circ Res* 1970;27:811–823.
32. Goto M, Brooks C. Membrane excitability of the frog ventricle examined by long pulses. *Am J Physiol* 1969;217:1236–1245.
33. Lindemans FW, Heethaar RM, van der Gon JJ, Zimmerman AN. Site of initial excitation and current threshold as a function of electrode radius in heart muscle. *Cardiovasc Res* 1975;9:95–104.
34. Ehara T. Rectifier properties of canine papillary muscle. *Jpn J Physiol* 1971; 21:49–69.
35. Latimer DC, Roth BJ. Electrical stimulation of cardiac tissue by a bipolar electrode in a conductive bath. *IEEE Trans Biomed Eng* 1998;45:1449–1458.
36. Roth BJ. Effect of a perfusing bath on the rate of rise of an action potential propagating through a slab of cardiac tissue. *Ann Biomed Eng* 1996;24:639–46.
37. Efimov IR, Cheng YN, Biermann M, et al. Transmembrane voltage changes produced by real and virtual electrodes during monophasic defibrillation shock

delivered by an implantable electrode. *J Cardiovasc Electrophysiol* 1997; 8:1031–1045.
38. Entcheva E, Eason J, Efimov IR, et al. Virtual electrode effects in transvenous defibrillation-modulation by structure and interface: Evidence from bidomain simulations and optical mapping. *J Cardiovasc Electrophysiol* 1998;9:949–961.
39. Wiggers CJ. The mechanism and nature of ventricular defibrillation. *Am Heart J* 1940;20:399.
40. Mower MM, Mirowski M, Spear JF, Moore EN. Patterns of ventricular activity during catheter defibrillation. *Circulation* 1974;49:858–861.
41. Zipes DP, Fischer J, King RM, et al. Termination of ventricular fibrillation in dogs by depolarizing a critical amount of myocardium. *Am J Cardiol* 1975;36:37–44.
42. Chen P-S, Shibata N, Dixon EG, et al. Comparison of the defibrillation threshold and the upper limit of ventricular vulnerability. *Circulation* 1986;73:1022–1028.
43. Dillon DM. Synchronized repolarization after defibrillation shocks. A possible component of the defibrillation process demonstrated by optical recording in rabbit heart. *Circulation* 1992;85:1865–1878.
44. Garfinkel A, Spano ML, Ditto WL, Weiss JN. Controlling cardiac chaos. *Science* 1992;257:1230–1235.
45. Garfinkel A, Chen PS, Walter DO, et al. Quasiperiodicity and chaos in cardiac fibrillation. *J Clin Invest* 1997;99:305–314.
46. Chen PS, Garfinkel A, Weiss JN, Karagueuzian HS. Spirals, chaos, and new mechanisms of wave propagation. *Pacing Clin Electrophysiol* 1997;20:414–421.
47. Davy JM, Fain ES, Dorian P, Winkle RA. The relationship between successful defibrillation and delivered energy in open-chest dogs: Reappraisal of the "defibrillation threshold" concept. *Am Heart J* 1987;113:77–84.
48. Sepulveda NG, Wikswo JP Jr, Echt DS. Finite element analysis of cardiac defibrillation current distributions. *IEEE Trans Biomed Eng* 1990;37:354–365.
49. Walcott GP, Knisley SB, Zhou X, et al. On the mechanism of ventricular defibrillation. *Pacing Clin Electrophysiol* 1997;20:422–431.
50. Chen P-S, Wolf PD, Ideker RE. Mechanism of cardiac defibrillation: A different point of view. *Circulation* 1991;84:913–919.
51. Witkowske FX, Penkoske PA, Plonsey R. Mechanism of cardiac defibrillation in open-chest dogs using unipolar DC-coupled simultaneous activation and shock potential recordings. *Circulation* 1990;82:244–260.
52. Roth BJ. The pinwheel experiment revisited. *J Theor Biol* 1998;190:389–393.
53. Kwaku KF, Dillon SM. Shock-induced depolarization of refractory myocardium prevents wave-front propagation in defibrillation. *Circ Res* 1996;79:957–973.
54. Plonsey R, Barr RC. Effect of microscopic and macroscopic discontinuities on the response of cardiac tissue to defibrillating (stimulating) currents. *Med Biol Eng Comput* 1986;24:130–136.
55. Krassowska W, Pilkington TC, Ideker RE. Periodic conductivity as a mechanism for cardiac stimulation and defibrillation. *IEEE Trans Biomed Eng* 1987;34:555–560.
56. Knisley SB, Blitchington TF, Hill BC, et al. Optical measurements of transmembrane potential changes during electric field stimulation of ventricular cells. *Circ Res* 1993;72:255–270.
57. Tung L, Sliz N, Mulligan MR. Influence of electrical axis of stimulation on excitation of cardiac muscle cells. *Circ Res* 1991;69:722–730.
58. Fast VG, Kléber AG. Cardiac tissue geometry as a determinant of unidirectional conduction block: Assessment of microscopic excitation spread by optical mapping in patterned cell cultures and in a computer model. *Cardiovasc Res* 1995;29:697–707.
59. Zhou X, Rollins DL, Smith WM, Ideker RE. Responses of the transmembrane potential of myocardial cells during a shock. *J Cardiovasc Electrophysiol* 1995;6:252–263.

60. Gillis AM, Fast VG, Rohr S, Kléber AG. Spatial changes in transmembrane potential during extracellular electrical shocks in cultured monolayers of neonatal rat ventricular myocytes. *Circ Res* 1996;79:676–690.
61. Trayanova NA, Roth BJ, Malden LJ. The response of a spherical heart to a uniform electric field: A bidomain analysis of cardiac stimulation. *IEEE Trans Biomed Eng* 1993;40:899–908.
62. Fishler MG. Syncytial heterogeneity as a mechanism underlying cardiac far-field stimulation during defibrillation-level shocks. *J Cardiovasc Electrophysiol* 1998;9:384–394.
63. Wikswo JP Jr, Lin S-F. The prompt response of the transmembrane potential distribution of rabbit epicardium to defibrillation-strength field stimulation. *Pacing Clin Electrophysiol* 1998;21:940.
64. Entcheva E. *Cardiac Tissue Structure-Electric Field Interactions in Polarizing the Heart: 3D Computer Models and Applications* [PhD dissertation]. Memphis, TN: University of Memphis; 1998.
65. Wikswo JP Jr. Tissue anisotropy, the cardiac bidomain, and the virtual cathode effect. In Zipes DP, Jalife J (eds): *Cardiac Electrophysiology: From Cell to Bedside.* Philadelphia: W.B. Saunders Co.; 1995:348–361.
66. Sepulveda NG, Wikswo JP Jr. Bipolar stimulation of cardiac tissue using an anisotropic bidomain model. *J Cardiovasc Electrophysiol* 1994;5:258–267.
67. Zhou X, Ideker RE, Blitchington TF, et al. Optical transmembrane potential measurements during defibrillation-strength shocks in perfused rabbit hearts. *Circ Res* 1995;77:593–602.
68. Lin S-F, Wikswo JP Jr. Endocardial defibrillation-strength stimulus produces bipolar responses and charge diffusion in rabbit left ventricle. *J Am Coll Cardiol* 1998;31:36A.
69. Trayanova NA, Roth BJ, Malden LJ. The response of a spherical heart to a uniform electric field: A bidomain analysis of cardiac stimulation. *IEEE Trans Biomed Eng* 1993;40:899–908.
70. Frazier DW, Wolf PD, Wharton JM, et al. Stimulus-induced critical point: Mechanism for electrical initiation of reentry in normal canine myocardium. *J Clin Invest* 1989;83:1039–1052.